Large interfacial spin-orbit torques in layered antiferromagnetic insulator NiPS3/ferromagnet bilayers

Schippers, C. F.; Swagten, H. J. M.; Guimaraes, M. H. D.

Published in:
Physical Review Materials

DOI:
10.1103/PhysRevMaterials.4.084007

Publication date:
2020

Large interfacial spin-orbit torques in layered antiferromagnetic insulator $NiPS_3$/ferromagnet bilayers

C. F. Schippers [1,*] H. J. M. Swagten,[1] and M. H. D. Guimarães [1,2,†]

[1]*Department of Applied Physics, Eindhoven University of Technology, P.O. Box 513, 5600 MB, Eindhoven, the Netherlands*

[2]*Zernike Institute for Advanced Materials, University of Groningen, P.O. Box 221, 9747 AG, Groningen, the Netherlands*

(Received 18 May 2020; revised 13 July 2020; accepted 4 August 2020; published 27 August 2020)

Finding efficient ways of manipulating magnetic bits is one of the core goals in spintronic research. Electrically-generated spin-orbit torques (SOTs) are good candidates for this and the search for materials capable of generating highly-efficient SOTs has gained a lot of traction in recent years. While antiferromagnet/ferromagnet bilayer structures have been employed extensively for passive applications, e.g., by using exchange bias fields, their active properties are not yet widely employed. Here we show the presence of large interfacial SOTs in the bilayer of a ferromagnet and the two-dimensional layered antiferromagnetic insulator $NiPS_3$. We observe a large in-plane dampinglike interfacial torque, showing a torque conductivity of $\sigma_{DL} \approx 1 \times 10^5 (\frac{\hbar}{2e})/(\Omega m)$ even at room temperature, comparable to the best devices reported in the literature for standard heavy-metal-based and topological insulators-based devices. Additionally, our devices also show an out-of-plane fieldlike torque arising from the $NiPS_3$/ferromagnet interface, further indicating the presence of an interfacial spin-orbit coupling in our structures. Temperature-dependent measurements reveal an increase of the SOTs with a decreasing temperature below the Néel temperature of $NiPS_3$ ($T_N \approx 170$ K), pointing to a possible effect of the magnetic ordering on our measured SOTs. Our findings show the potential of antiferromagnetic insulators and two-dimensional materials for future spintronic applications.

DOI: 10.1103/PhysRevMaterials.4.084007

I. INTRODUCTION

The electrical manipulation of magnetization is a promising approach for novel nonvolatile and energy efficient memory devices. An especially efficient approach uses current-induced spin-orbit torques (SOTs) [1,2], where an electric current flows through a material with high spin-orbit coupling, which applies a torque on an interfaced magnetic material. These torques can arise from bulk effects, such as the spin-Hall effect [3,4], where the electrons in a charge current flowing through a conducting layer get deflected to opposite directions depending on their spin. This is the main mechanism for current-induced SOTs in heavy metal/ferromagnet bilayer structures, such as Pt/permalloy ($Ni_{80}Fe_{20}$; Py) [1]. Interfacial effects, such as the Rashba-Edelstein effect [5,6], can also generate a sizable charge-to-spin conversion and can be used for SOT generation [7–9]. More recently, it has been shown that when SOTs are generated in metallic ferromagnetic [10–12] and antiferromagnetic materials [13–15], the magnetic ordering can be used to control the direction and magnitude of the generated SOTs [16]. Even though magnetic insulators have been investigated extensively for the generation of spin currents via spin-pumping [17,18] and spin Seebeck effects [19,20], the use of antiferromagnetic insulators in spin-orbit torque devices remains vastly unexplored.

$NiPS_3$ is a layered semiconducting antiferromagnetic van der Waals crystal with a Néel transition temperature of approximately 170 K in its bulk form [21]. Below the transition temperature the magnetic moments of the hexagonally-arranged Ni atoms align in a zigzag fashion, where the coupling is ferromagnetic along a zigzag line and antiferromagnetic across it [22]. Due to its semiconducting nature and relatively flat band dispersion, $NiPS_3$ presents a very high resistivity unless heavily doped or under ultraviolet (UV) light illumination [23,24]. Moreover, $NiPS_3$ also presents promising efficient catalytic properties for hydrogen evolution reaction. Therefore, its main applications so far have been focused on UV light detectors and electrocatalysis [25].

Layered van der Waals materials coupled with 3D ferromagnets have recently been used to explore SOTs, demonstrating promising efficiencies and interesting effects [26–31]. In particular, monolayers of two-dimensional semiconductors have shown large interfacially-generated SOTs [26,27,29,30]. Moreover, it has been shown that layered van der Waals materials possessing low crystal symmetry can give rise to SOTs which are in principle forbidden by symmetry in standard systems, such as Pt/Py [28,29]. However, the microscopic mechanisms behind the generation of SOTs in van der Waals materials are still poorly understood. It is theoretically predicted that SOTs with interfacial origins can give rise to both fieldlike (τ_{FL}) and dampinglike (τ_{DL}) SOTs [7,8]. These torques usually have forms $\tau_{FL} \propto \hat{m} \times \hat{y}$ and $\tau_{DL} \propto \hat{m} \times (\hat{m} \times \hat{y})$, where $\hat{m}$ indicates the magnetization direction and $\hat{y}$ points in the direction perpendicular to the charge current.

*c.f.schippers@tue.nl

†m.h.guimaraes@rug.nl

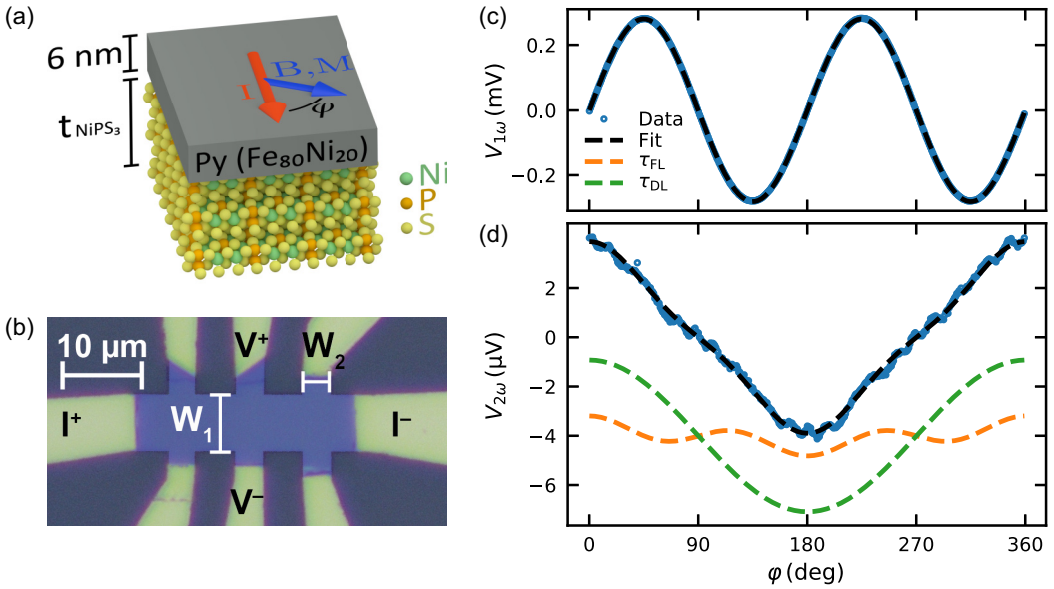

FIG. 1. Sample geometry and typical measurements. (a) Schematic of the $NiPS_3$/Py bilayers used in the second-harmonic Hall measurements. (b) Optical micrograph of a typical Hall bar device used (device D1). The light blue region in the center is the Hall bar, patterned from $NiPS_3$/Py/Al(Ox); the golden regions are the Au-covered contact leads. Colors have been enhanced for clarity. First- (c) and second- (d) harmonic Hall voltage as a function in-plane magnetic field angle φ, at room temperature (300 K) and a magnetic field of 34 mT for device D1. The first-harmonic Hall voltage is fitted with Eq. (1) and the second-harmonic with Eq. (2), where the individual contributions of τ_{FL} and τ_{DL} are separately shown, with an arbitrary offset. For both harmonics, a constant background has been removed.

Here we show that a $NiPS_3$/Py bilayer device can also provide large current-induced interfacial SOTs at room temperature, with an in-plane dampinglike interfacial torque comparable to the best topological insulators/ferromagnet [32] and heavy-metal (e.g., Pt)/ferromagnet devices [1]. In addition to the in-plane dampinglike torque we also observe a weaker out-of-plane fieldlike torque which also is of interfacial nature. Temperature-dependent measurements across the Néel temperature of $NiPS_3$ show an increasing SOT efficiency, for both in-plane dampinglike and out-of-plane fieldlike torques, indicating a possible influence of the magnetization ordering of $NiPS_3$ on the SOTs [33]. Our results demonstrate a promising route for the use of (layered) antiferromagnetic insulators for efficient manipulation of magnetic bits.

Our devices are schematically shown in Fig. 1(a). The device preparation is described in detail in the Methods section. In short, thin $NiPS_3$ crystals are mechanically exfoliated from a commercially available $NiPS_3$ crystal (HQ graphene). The exfoliation is performed in vacuum, with pressures $<10^{-6}$ mbar, to maintain a high interface quality of the $NiPS_3$ flakes. Without breaking vacuum, 6 nm of Py is sputter deposited on the sample followed by a thin 1.5 nm Al capping layer which was naturally oxidized after exposing the samples to atmosphere. The thickness and flatness of the flakes is characterized using atomic force microscopy (AFM). All the selected flakes for device fabrication showed a roughness below 0.5 nm root-mean-square (RMS) in AFM images. In the main text we focus on two devices with different values for $NiPS_3$ layer thickness: device D1, where the $NiPS_3$ flake has a thickness of $t_{NPS} = 3.15$ nm, and device D2, with $t_{NPS} = 6.34$ nm, corresponding to four and nine layers of $NiPS_3$ [34], respectively. Measurements for one additional device and for different current-voltage configurations can be found in the Supplemental Material [35]. The Hall bars were then defined using standard electron-beam lithography and ion-beam milling techniques, followed by another lithography step and electron-beam evaporation to define the Ti(10 nm)/Au(100 nm) leads. Figure 1(b) shows an optical micrograph of a finished device.

II. RESULTS AND DISCUSSION

The harmonic Hall measurements were performed using standard low-frequency (17 Hz) lock-in techniques. A current $I_0 \approx 2.5$ mA was driven between the outer contacts and the induced Hall voltage, in the first ($V_H^{1\omega}$) and second ($V_H^{2\omega}$) harmonic of the frequency used, was detected between the arms of the Hall bar. Simultaneously, a magnetic field $\boldsymbol{B}$ was applied in the sample plane under an angle φ with respect to the current direction [Fig. 1(a)]. Assuming the magnetization $\boldsymbol{M}$ of the Py layer aligns to the external magnetic field, $V_H^{1\omega}$ is given by:

$$V_H^{1\omega} = I_0 R_P \sin 2\varphi \sin^2 \vartheta + I_0 R_A \cos \vartheta, \quad (1)$$

where ϑ is the polar angle of the magnetic field (i.e., the angle with respect to the sample normal), R_P is the planar Hall resistance, and R_A is the anomalous Hall resistance.

The first harmonic Hall voltage as a function of φ for a fixed value of $B = 34$ mT at room temperature (300 K) for device D1 is shown in Fig. 1(c) as an example of a typical measurement (other measurements on both the same device and other devices have similar signal-to-noise ratios and curve fitting quality). The measurement is corrected for a small phase offset caused by a small misalignment of the current direction with the x axis of our experimental setup. We observe a $\sin(2\varphi)$ behavior with the values for R_P in our

devices obtained by fitting our measurement using Eq. (1). Similarly, we extract the value for R_A through out-of-plane magnetic field measurements, as detailed in the Supplemental Material [35]. The values R_P and R_A are used to quantify the measured spin-torque values that we discuss later in the text.

Bulk $NiPS_3$ belongs to the symmetry group $C2/m$ in its paramagnetic state [22,34,36,37], presenting one rotation axis, a glide mirror plane, and an inversion point. Below the Néel transition temperature, the magnetic texture further reduces the symmetries of the bulk to a single mirror plane, space group Pm [22]. Therefore, one could expect an induced magnetic anisotropy as reported for the low-symmetry layered materials (e.g., WTe_2 and $TaTe_2$) [28,29,31]. Moreover, the antiferromagnetic ordering of $NiPS_3$ could also induce an exchange bias on the Py if the magnetic structure is not strictly collinear or a small exchange bias via a perpendicular coupling at the interface of the antiferromagnetic spins of $NiPS_3$ and the ferromagnetic spins of Py [38]. In the measurement shown in Fig. 1(c) we do not find a significant deviation from the fit with Eq. (1), which does not take into account any anisotropy or exchange bias. Hence, we do not observe an induced magnetic anisotropy or exchange bias induced by our $NiPS_3$ crystals (see Supplemental Material for further measurements [35]). The lack of an induced in-plane magnetic anisotropy is in agreement with measurements in devices based on high-symmetry transition metal dichalcogenide (TMD) crystals [26,27,30]. This indicates that the magnetic anisotropy as observed in the low-symmetry materials is most likely strongly dependent on the specifics of the electronic properties and exchange coupling of the bilayer structure. Moreover, the lack of an observable exchange bias upon field cooling the device through the Néel temperature agrees with the expected collinear magnetic ordering in our $NiPS_3$ crystals.

In addition to a first harmonic response, the presence of a non-negligible current-induced SOT gives rise to a Hall voltage in the second harmonic of the current [39,40]. Assuming that the magnetization direction follows the applied magnetic field, the second harmonic Hall voltage $V_H^{2\omega}$ is given by [29]:

$$V_H^{2\omega} = -I_0 R_P C_{FL} \cos 2\varphi \cos\varphi - \frac{1}{2} I_0 R_A C_{DL} \cos\varphi, \qquad (2)$$

where C_{FL} and C_{DL} are coefficients proportional to the out-of-plane fieldlike and in-plane dampinglike torques and given by $C_{FL} = \frac{\tau_{FL}}{\gamma B}$, and $C_{DL} = \frac{\tau_{DL}}{\gamma(B+B_K)} + \frac{2V_{ANE}}{I_0 R_A}$. Here γ is the gyromagnetic ratio and B_K the total effective anisotropy field, including demagnetization and anisotropy terms, and V_{ANE} is the anomalous Nernst contribution.

Figure 1(d) shows a typical measurement of the second harmonic Hall voltage as a function of the in-plane magnetic field angle φ. The contributions by the different torques τ_{FL} and τ_{DL} can be obtained by fitting our data using the equation above, and their individual contributions to the fit are shown in Fig. 1(d). To disentangle other unwanted contributions on our signals, such as the anomalous Nernst effect [27], we perform angular dependence measurements for various values of applied magnetic field [41,42].

Figure 2 shows second harmonic Hall measurements for various values of the external magnetic field strength and temperatures. Here we see that the line shape of the second

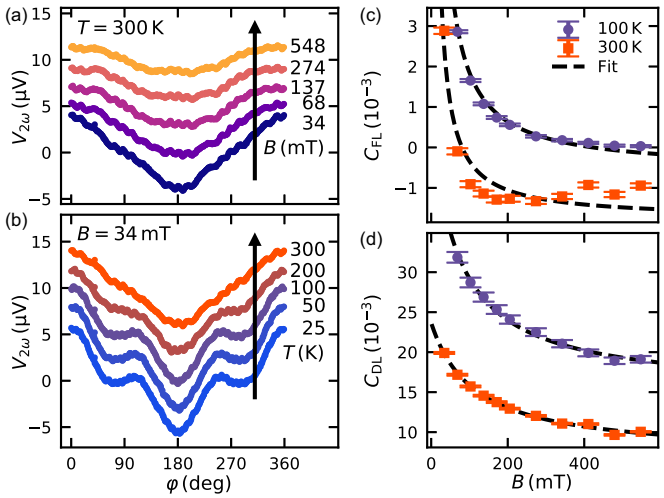

FIG. 2. Field and temperature dependence of the second-harmonic Hall voltage. The second-harmonic Hall voltage $V_{2\omega}$ is measured as a function of in-plane field angle φ for a number of magnetic field strengths B (a) and temperatures (b). For clarity an arbitrary offset has been added to the measurements. (c) and (d) show the magnetic field dependence of coefficients C_{FL} and C_{DL} for different temperatures. The fits are performed as described in the text.

harmonic Hall measurement changes with both the external magnetic field for a fixed temperature [Fig. 2(a)], and as a function of temperature for a fixed magnetic field [Fig. 2(b)], indicating a change in weight for the different contributions for τ_{DL} and τ_{FL} in our devices. We fit the angle-dependent measurements for different fields and temperatures using Eq. (2). There we include a constant offset to account for terms unrelated to current-induced spin-orbit torque such as thermal effects (anomalous Nernst effect) [27], and use R_A and R_P as determined earlier. Values for the coefficients C_{FL} and C_{DL} are obtained for each individual measurement, shown in Figs. 2(c) and 2(d). The current-induced SOTs are then quantified by fitting C_{FL} and C_{DL}, as described earlier, shown as dashed lines in Figs. 2(c) and 2(d), to extract τ_{FL} and τ_{DL}. It has been reported that spin-orbit torque measurements using the second harmonic Hall technique can be influenced by the aspect ratio of the Hall bar dimensions [W_2/W_1 as specified in Fig. 1(a)] [43]. Therefore, in order to better quantify our results, the values for the torques (i.e., τ_{FL} and τ_{DL}) we obtained were corrected for our specific Hall bar geometry by dividing the torque value by a factor corresponding to the Hall bar geometry [44].

At room temperature (300 K) we observe an in-plane dampinglike $[\hat{m} \times (\hat{m} \times \hat{y})]$ torque $\tau_{DL}/(\gamma I_0) = (1.0 \pm 0.1)$ mT/mA, for device D1. For a better comparison between our devices and others in literature, the spin orbit torque can be normalized by the electric field (E) applied to the device, $\tau_{DL}/(\gamma E)$. The torque value can also be evaluated as torque conductivity σ, defined as the angular momentum absorbed by the magnet per second per unit interface area per unit electric field. For a torque τ_i (i= DL or FL), we calculate the corresponding spin-torque conductivity by $\sigma = M_S t_{FM} \frac{W_1}{R_S} \frac{\tau_i}{\gamma I_0}$, where M_S is the saturation magnetization of

TABLE I. The torque conductivities σ_{FL} and σ_{DL} [in 10^5 $(\frac{\hbar}{2e})/(\Omega m)$] is given at both room temperature (RT, 300 K) and low temperature (LT, 50 K), assuming a saturation magnetization of $\mu_0 M_S = 0.7$ T. Also the dimensions of the Hall bars (W_1 and W_2 in μm as defined in Fig. 1), the thickness of the $NiPS_3$ flake t_{NPS} (in nm), with the estimated number of layers n [34] between brackets, and the sheet resistance R_S^{RT} (in Ω/sq) at room temperature are given.

Device	W_1	W_2	t_{NPS} (n)	R_S^{RT}	σ_{FL}^{RT}	σ_{FL}^{LT}	σ_{DL}^{RT}	σ_{DL}^{LT}
D1	3.0	2.5	3.1 (4)	140.7	0.17 ± 0.02	0.319 ± 0.004	2.2 ± 0.03	3.2 ± 0.3
D2	3.0	2.0	6.3 (7)	151.8	0.1 ± 0.1	-2.32 ± 0.08	0.6 ± 0.1	10 ± 2
D3	3.0	2.0	5.2 (9)	144.3		-2.01 ± 0.08		8 ± 1
Pt/Py	5.0	3.0		15.1	7.76 ± 0.03	8.99 ± 0.03	7.3 ± 0.3	8 ± 1
Py	5.0	3.0		112.0	0.0921 ± 0.0009		-0.079 ± 0.0099	

the Py FM layer, $t_{FM} = 6$ nm is the thickness of the Py layer, W_1 is the Hall bar width as defined in Fig. 1(a), and R_S is the sheet resistance of the measured device; torque conductivities for various devices are summarized in Table I. We obtain $\tau_{DL}/(\gamma E) = (22 \pm 3)$ nm T/V and $\sigma_{DL} = (2.2 \pm 0.3) \times 10^5 (\frac{\hbar}{2e})/(\Omega m)$ for the in-plane dampinglike torque τ_{DL}, using $\mu_0 M_S = 0.7$ T as discussed in the Supplemental Material [28–31,35]. This is the largest dampinglike torque conductivity for all layered material/ferromagnet devices reported so far, which are over one order of magnitude lower [26–31,45], and is in the range of the best values obtained using standard heavy-metal/ferromagnet devices and topological insulator/ferromagnet devices, in the order of 1×10^5 $(\frac{\hbar}{2e})/(\Omega m)$ [32,41,46].

We also find a non-negligible out-of-plane fieldlike torque $(\hat{m} \times \hat{y})$ in our $NiPS_3$/Py devices, $\tau_{FL}/(\gamma I_0) = (0.079 \pm 0.009)$ mT/mA at room temperature, corresponding to $\tau_{FL}/(\gamma E) = (1.7 \pm 0.2)$ nm T/V and a spin-torque conductivity of $\sigma_{FL} = (1.7 \pm 0.2) \times 10^4$ $(\frac{\hbar}{2e})/(\Omega m)$. The presence of both dampinglike and fieldlike torques arising from interfacial SOTs are in agreement with theoretical predictions [7,8]. However, the magnitude for τ_{FL} is about one order of magnitude smaller than the dampinglike torques discussed above.

To understand where the observed torque originates from it is instructive to consider the possible current paths through the $NiPS_3$/Py bilayer. Intrinsic $NiPS_3$ is highly resistive [23,24], in sharp contrast to the metallic Py layer, which has a resistivity that is orders of magnitude lower than $NiPS_3$ (of the order of 10^{-5} Ω cm for Py compared to 10^{11} Ω cm for $NiPS_3$). Hence, we expect that all current flows through the Py layer in our $NiPS_3$/Py devices. This is confirmed by measurements of the sheet resistances R_S for $NiPS_3$/Py based devices (140 to 150 Ω/sq) and a Py based device (∼110 Ω/sq), i.e., without a SOT material layer. The small difference in sheet resistance could be attributed to a difference in quality of the Py layer when grown on top of the different surfaces, the $NiPS_3$ flake or the bare Si/SiO_2 substrate. Hence, the torques measured have to arise from the interface between Py and $NiPS_3$; the large values for τ_{DL} observed in our devices indicate the presence of a very strong interfacial SOT.

Other possible contributions to the observed SOTs can arise from the Al capping layer. If the Al capping layer is not completely oxidized, a current path through the Al capping layer allows the generation of an Oersted field working on the Py layer. Alternatively, when a current flows through the Py layer in an inhomogeneous manner, the Oersted field generated by the current through the Py layer does not fully cancel and a net out-of-plane fieldlike torque can be measured. In order to probe such possible contributions on our results we perform control measurements in devices based on a single Py layer, without a SOT material, but still capped with the naturally-oxidized Al(1.5 nm) layer. For these samples we obtained $\tau_{DL}/(\gamma E) = (-0.78 \pm 0.09)$ nm T/V, considerably smaller (and of opposite sign) than the values obtained in our $NiPS_3$ devices. Interestingly, we also observe a measurable, albeit smaller, τ_{FL} for Hall bars based on only Py $\tau_{FL}/(\gamma E) = (0.91 \pm 0.09)$ nm T/V, i.e., without a spin-orbit torque generating material. This unexpected torque could be an indication of an additional contribution from either an unoxidized portion of the Al capping layer or an inhomogeneous current distribution in the ferromagnetic layer. However, as the SOTs observed in this device are significantly smaller than the SOTs observed in the $NiPS_3$ devices, this shows that the Al oxide capping layer has a minimal effect on our measured torque values and points to the crucial role of the $NiPS_3$ flake on the measured spin-orbit torques in those devices.

We also perform a direct comparison to standard heavy-metal/ferromagnet SOT devices by performing control measurements in a Pt/Py device fabricated using the same procedure as the $NiPS_3$ devices. For these devices we obtain $\tau_{DL}/(\gamma E) = (72 \pm 3)$ nm T/V. This translates to a torque conductivity $\sigma_{DL} = (7.3 \pm 0.3) \times 10^5 (\frac{\hbar}{2e})/(\Omega m)$, which is in line with the typical torques observed in literature [32,41,46]. This torque is only slightly larger than the torque found in the $NiPS_3$ based device, illustrating that the torque found in the $NiPS_3$ based device is indeed in the range of the best heavy-metal based or topological insulator based devices. Finally, for our Pt/Py devices we observe a $\tau_{FL}/(\gamma E) = (76.4 \pm 0.3)$ nm T/V, with a magnitude consistent with the expected Oersted-field contribution from the current flowing in the Pt layer.

Even though a significant out-of-plane fieldlike torque is observed in all our devices, there is a clear difference between the results in our control Py and Pt/Py devices and the ones for the $NiPS_3$/Py devices: While Py and Pt/Py devices consistently show a positive sign for τ_{FL}, we observe both positive and negative signs for our $NiPS_3$/Py devices (see Supplemental Material for more measurements [35]). The presence of an interfacial out-of-plane fieldlike torque has been observed in devices based on TMD monolayers [27], with a sign change with respect to Oersted fields observed in monolayer $NbSe_2$/Py bilayers [30]. Albeit we cannot completely rule out the possibility of alternative mechanisms for the observed

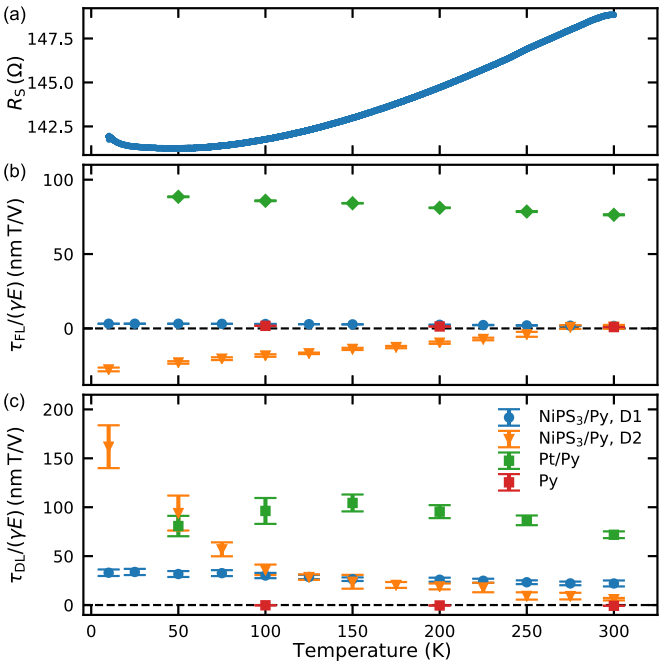

FIG. 3. Torques as a function of temperature. (a) Sheet resistance R_S of the $NiPS_3$/Py/Al(Ox) Hall bar as a function of temperature. Out-of-plane fieldlike torque τ_{FL} (b) and in-plane dampinglike torque τ_{DL} (c) as a function of temperature in the $NiPS_3$/Py bilayer devices, a Py reference sample, and a Pt/Py reference sample. The measured torques have been corrected for influence of the Hall bar geometry, according to Ref. [43], and normalized by the applied electric field for better comparison among devices.

τ_{FL}, such as an inhomogeneous current distribution in the Py layer, the comparison of the results for the three different devices (Py, Pt/Py, and $NiPS_3$/Py) indicate the presence of a non-negligible interfacial out-of-plane fieldlike torque.

In order to explore the effect of the antiferromagnetic phase transition of $NiPS_3$ on the current-induced SOTs we performed measurements as a function of temperature across $T_N \sim 170$ K, with T ranging from 10 K to 300 K. Our devices show a decrease in sheet resistance of about 5% with a decrease in temperature indicating a metallic behavior [Fig. 3(a) for device D1], in agreement with the expectation that the resistance in our devices is dominated by the metallic Py layer.

By performing the same procedure for quantifying τ_{DL} and τ_{FL} described above, we extract the temperature dependence of the spin-orbit torques [Figs. 3(b) and 3(c) for τ_{DL} and τ_{FL}, respectively]. In Table I the torque conductivities at room temperature and low temperature are summarized for all devices. We observe that there is indeed a temperature dependence of both the out-of-plane fieldlike and in-plane dampinglike torques; in device D1 the torques increase up to (3.16 ± 0.3) nm T/V and (33 ± 3) nm T/V when lowering the temperature to 10 K for the out-of-plane fieldlike and in-plane dampinglike torques, respectively. For the in-plane dampinglike torque this behavior is consistent over different devices: The torque value increases when the temperature decreases, though the amount of increase is not constant over the different devices (see Supplemental Material [35]). We find no consistent behavior for the out-of-plane fieldlike torque in our $NiPS_3$/Py devices apart from the fact that the torque magnitude and sign seem to be strongly dependent on temperature (see Supplemental Material [35]).

The increase for the in-plane dampinglike torque with a decrease in temperature seems reproducible among our $NiPS_3$/Py devices, however, we find that the specific trend with temperature is device specific. For device D2, for example, we observe a smaller in-plane dampinglike torque at room temperature $[\tau_{DL}/(\gamma E) = (6 \pm 1)$ nm T/V] and a much steeper increase to (160 ± 20) nm T/V at 10 K, significantly larger than the maximum value in device D1. Interestingly, for all our devices we see an onset on the change in torque magnitude at temperatures near the Néel temperature of $NiPS_3$, around 150 K. Even though this is a qualitative observation, we believe that this is an indication that the magnetic ordering in $NiPS_3$ has an effect on the measured SOTs. However, further research is required to confirm whether or not the magnetic order of $NiPS_3$ is responsible for (part of) the observed temperature dependence.

The behavior of the out-of-plane fieldlike torque τ_{FL} is different for different devices. For some devices we observe a negative value for τ_{FL} that also increases in magnitude when the temperature is decreased while others show an initially positive torque that changes sign when the temperature is decreased. The reason for these different temperature dependencies (for both the in-plane dampinglike and out-of-plane fieldlike torque) remains unclear and requires further studies. Possible explanations might be related to the thickness of the $NiPS_3$ flake—device D1 contains a relatively thin flake of only four layers of $NiPS_3$ while device D2 contains a flake of nine layers—or to the quality of the interface between the $NiPS_3$ flake and the Py layer, which could, e.g., result in a temperature-dependent spin-mixing conductance. Although devices with three different $NiPS_3$ thicknesses were measured and both similarities and differences were found, we did not observe a systematic behavior with thickness. A more systematic study on the thickness dependence is required and is left for future investigations.

We now compare the temperature dependence of the SOTs obtained for our $NiPS_3$/Py to our control Pt/Py and Py devices, Figs. 3(b) and 3(c). For the Py based device we observe a very small change in both τ_{FL} and τ_{DL}, with values close to zero throughout the whole measured temperature range. For the Pt/Py device we find a small monotonic increase of τ_{FL} with a decrease in temperature, probably indicating that the Pt layer decreases its resistivity faster than the Py layer, therefore increasing the Oersted-field torque in this device. We also observe a small change in τ_{DL} with a change in temperature but different from the monotonic increase observed for our $NiPS_3$/Py devices. This strengthens the conclusion that both the SOTs observed in the $NiPS_3$/Py devices and their temperature dependence originate from the $NiPS_3$/Py interface.

While the exact origin of the observed spin-orbit torque in the $NiPS_3$/Py devices is not understood at this moment, we suggest two possible mechanisms. First, the inversion symmetry breaking at the $NiPS_3$/Py interface can allow for the presence of a Rashba spin-orbit coupling. This effect has been shown to give rise to strong SOTs in metallic [2], topological-insulators [2,32], and TMD-based devices [28,29]. Alternatively, a noncollinearity of the antiferromagnetic order in

$NiPS_3$ or the ferromagnetic ordering in Py could allow for effective SOTs to be generated even in the absence of a spin-orbit interaction in the $NiPS_3$ [33]. Though both $NiPS_3$ and Py present fully collinear magnetic structures, their mutual exchange interaction can lead to a spatially-varying magnetic ordering, thereby adding a small noncollinear contribution to the magnetic order. However, a more in-depth understanding of the nature of the mechanisms involved in generating the observed SOTs requires a more thorough theoretical treatment.

We point out that intermixing or a magnetic dead layer at the interface between Py and $NiPS_3$ can also affect the torques. It has recently been demonstrated that a single Py layer can also generate SOTs in an asymmetric stack [47]. These anomalous spin-orbit torques are strongly dependent on the properties of both interfaces and at this moment their contribution in previously measured spin-orbit torques is still unclear. However, the net torques estimated for insulator/thin Py/insulator structures were still one order of magnitude smaller than the torques measured here. A careful thickness dependence combined with cross-sectional transmission electron microscopy could help to clarify the importance of such effects in future works.

Below the Néel temperature, $NiPS_3$ presents an antiferromagnetic ordering (with ferromagnetic zigzag lines that couple antiferromagnetically) [22] which breaks the glide mirror plane and the screw symmetry axis. It has been shown that a crystallographic (or magnetic) symmetry breaking can lead to nonstandard spin-orbit torques [14,28,29,31,33,45]. In order to explore a possible effect of the crystal and magnetic symmetries and orientation on the measured SOTs, we perform the fitting procedure with extra terms representing an out-of-plane dampinglike torque ($\hat{m} \times \hat{m} \times \hat{z}$). Additionally, we performed the same measurements and analysis with the current and voltage paths interchanged, i.e., rotated by $\pi/2$. Here the angle between the current and the zigzag line of the magnetic ordering should change for the two configurations which could have an influence on the torques that are generated by the $NiPS_3$/Py interface. We observe only a small difference of a factor of approximately 1.5 in τ_{DL} and smaller for τ_{FL} (see Supplemental Material [35]). As this is reproduced in our control devices it likely arises from the different current paths for the two configurations and seems to be unrelated to the crystal properties of $NiPS_3$. Therefore, no torque components related to the crystal and magnetic symmetries and orientation are observed within our experimental accuracy.

III. CONCLUSION

In conclusion, we observe large interfacial in-plane dampinglike SOTs in $NiPS_3$/Py bilayers. Our devices present in-plane dampinglike SOTs in the order of $\tau_{DL}/(\gamma E) = 20\,\mathrm{nm\,T/V}$ and $80\,\mathrm{nm\,T/V}$ at room and low temperatures, respectively, compared to $70\,\mathrm{nm\,T/V}$ found at a heavy-metal/ferromagnet device (Pt/Py). Additionally, we observe a small interfacial out-of-plane fieldlike SOT of $\tau_{FL}/(\gamma E) = 2\,\mathrm{nm\,T/V}$ with a direction that is opposite to a torque from Oersted fields coming from a current through the $NiPS_3$ flake, which is in line with the high resistivity of $NiPS_3$ that prevents a current from running through the flake. Though we observed a (nontrivial) temperature dependence of the observed SOTs, we found no clear relation to the antiferromagnetic phase transition of $NiPS_3$ or the related reduction of the crystallographic symmetry. Based on these findings, we conclude that there is a significant contribution of the interface between $NiPS_3$ and Py to both the out-of-plane fieldlike and in-plane dampinglike SOTs, although the microscopic origin is not yet understood.

Our results add to the understanding that the detailed electronic structure of the interface between the spin-orbit material and ferromagnet plays a critical role on the measured SOTs and should encourage the development of a more complete theoretical framework for the prediction of SOTs using various materials. The large interfacial torque and lack of dependence on the specific crystal symmetries or orientation is ideal for highly-efficient SOT devices. The fact that current flows only through the ferromagnetic layer allows for the use of lower total currents for magnetization switching when compared to standard heavy-metal/ferromagnet devices. Therefore, we believe our results illustrate the potential of insulating van der Waals crystals for spintronic applications.

IV. METHODS

Sample fabrication

$NiPS_3$ flakes were mechanically exfoliated from commercially available crystals (HQ graphene) onto a thermally oxidized Si/SiO_2 substrate (with 100 nm SiO_2). For this exfoliation ordinary scotch tape was used. To prevent degradation of the flakes and conserve the high-quality interface of the exfoliated flakes the exfoliation is performed in two steps. First the tape with flakes is prepared and placed on the substrate in a nitrogen-filled glovebox. The substrate, with tape, is transported (through air) to the load lock of the deposition system. Here, the actual exfoliation is performed when the load lock has reached a pressure $<10^{-6}$ mbar.

The sample is then immediately transported, through vacuum, into the deposition chamber, where Py(6)/Al(1.5) is deposited on the sample by magnetron sputtering. Afterwards, the sample is taken out of the vacuum into air, where the Al layer will oxidize to Al_2O_3, creating an insulating and protective layer for the sample. Using an optical microscope the sample is inspected to find sufficiently large (i.e., larger than 5 μm × 5 μm) $NiPS_3$ flakes for later sample fabrication.

For each sufficiently large flake a Hall bar is designed and patterned into a SiO_2 hard mask using electron-beam lithography (EBL) with poly-(methyl-methacrylate) (PMMA), sputter deposition of SiO_2 (60 nm), and a liftoff process. The Hall bar is then etched into the $NiPS_3$ flake using argon (Ar) ion-beam milling; a layer of SiO_2 (20 nm) is sputter deposited to clamp the Hall bars on the sample.

Hereafter the Hall bars contacts are fabricated. The contacts are patterned into a layer of PMMA, again using EBL. Using reactive ion etching the SiO_2 layer is removed in places where the contacts will be deposited. Finally, Ti/Au is deposited for the contacts, after a short argon etching to remove the Al_2O_3 on top of the Py for better contacts, and liftoff is performed to remove the PMMA and the redundant Ti/Au.

ACKNOWLEDGMENTS

We acknowledge B. Koopmans, M. J. Grzybowski, and M. Titov for fruitful discussions and for useful comments on the paper and J. Francke and G. Basselmans for technical help with the experimental setup. Sample fabrication was performed using NanoLabNL facilities. The research performed here was funded by the Dutch Research Council (NWO) under Grants No. VENI 15093 and No. 680-91-113.

C.F.S. and M.H.D.G. conceived the experiment, fabricated the samples, and performed the measurements while advised by H.J.M.S. C.F.S. performed the data analysis under M.H.D.G. and H.J.M.S. supervision. C.F.S. and M.H.D.G. wrote the paper with comments from H.J.M.S.

[1] L. Liu, T. Moriyama, D. C. Ralph, and R. A. Buhrman, Spin-Torque Ferromagnetic Resonance Induced by the Spin Hall Effect, Phys. Rev. Lett. **106**, 036601 (2011).

[2] A. Manchon, H. C. Koo, J. Nitta, S. M. Frolov, and R. A. Duine, New perspectives for Rashba spin-orbit coupling, Nat. Mater. **14**, 871 (2015).

[3] P. P. Haazen, E. Murè, J. H. Franken, R. Lavrijsen, H. J. Swagten, and B. Koopmans, Domain wall depinning governed by the spin Hall effect, Nat. Mater. **12**, 299 (2013).

[4] A. van den Brink, G. Vermijs, A. Solignac, J. Koo, J. T. Kohlhepp, H. J. M. Swagten, and B. Koopmans, Field-free magnetization reversal by spin-Hall effect and exchange bias, Nat. Commun. **7**, 10854 (2016).

[5] V. M. Edelstein, Spin polarization of conduction electrons induced by electric current in two-dimensional asymmetric electron systems, Solid State Commun. **73**, 233 (1990).

[6] A. Chernyshov, M. Overby, X. Liu, J. K. Furdyna, Y. Lyanda-Geller, and L. P. Rokhinson, Evidence for reversible control of magnetization in a ferromagnetic material by means of spin-orbit magnetic field, Nat. Phys. **5**, 656 (2009).

[7] V. P. Amin and M. D. Stiles, Spin transport at interfaces with spin-orbit coupling: Formalism, Phys. Rev. B **94**, 104419 (2016).

[8] V. P. Amin and M. D. Stiles, Spin transport at interfaces with spin-orbit coupling: Phenomenology, Phys. Rev. B **94**, 104420 (2016).

[9] F. Hellman, A. Hoffmann, Y. Tserkovnyak, G. S. D. Beach, E. E. Fullerton, C. Leighton, A. H. MacDonald, D. C. Ralph, D. A. Arena, H. A. Dürr, P. Fischer, J. Grollier, J. P. Heremans, T. Jungwirth, A. V. Kimel, B. Koopmans, I. N. Krivorotov, S. J. May, A. K. Petford-Long, J. M. Rondinelli, N. Samarth, I. K. Schuller, A. N. Slavin, M. D. Stiles, O. Tchernyshyov, A. Thiaville, and B. L. Zink, Interface-induced phenomena in magnetism, Rev. Mod. Phys. **89**, 025006 (2017).

[10] K. S. Das, J. Liu, B. J. Van Wees, and I. J. Vera-Marun, Efficient Injection and Detection of Out-of-Plane Spins via the Anomalous Spin Hall Effect in Permalloy Nanowires, Nano Lett. **18**, 5633 (2018).

[11] J. D. Gibbons, D. MacNeill, R. A. Buhrman, and D. C. Ralph, Reorientable Spin Direction for Spin Current Produced by the Anomalous Hall Effect, Phys. Rev. Applied **9**, 064033 (2018).

[12] C. Safranski, E. A. Montoya, and I. N. Krivorotov, Spin–orbit torque driven by a planar Hall current, Nat. Nanotechnol. **14**, 27 (2019).

[13] J. Zhou, X. Wang, Y. Liu, J. Yu, H. Fu, L. Liu, S. Chen, J. Deng, W. Lin, X. Shu, H. Y. Yoong, T. Hong, M. Matsuda, P. Yang, S. Adams, B. Yan, X. Han, and J. Chen, Large spin-orbit torque efficiency enhanced by magnetic structure of collinear antiferromagnet IrMn, Sci. Adv. **5**, eaau6696 (2019).

[14] W. Zhang, W. Han, S. H. Yang, Y. Sun, Y. Zhang, B. Yan, and S. S. Parkin, Giant facet-dependent spin-orbit torque and spin Hall conductivity in the triangular antiferromagnet IrMn3, Sci. Adv. **2**, e1600759 (2016).

[15] V. Tshitoyan, C. Ciccarelli, A. P. Mihai, M. Ali, A. C. Irvine, T. A. Moore, T. Jungwirth, and A. J. Ferguson, Electrical manipulation of ferromagnetic NiFe by antiferromagnetic IrMn, Phys. Rev. B **92**, 214406 (2015).

[16] A. Davidson, V. P. Amin, W. S. Aljuaid, P. M. Haney, and X. Fan, Perspectives of electrically generated spin currents in ferromagnetic materials, Phys. Lett. A **384**, 126228 (2020).

[17] E. Saitoh, M. Ueda, H. Miyajima, and G. Tatara, Conversion of spin current into charge current at room temperature: Inverse spin-Hall effect, Appl. Phys. Lett. **88**, 182509 (2006).

[18] B. Heinrich, C. Burrowes, E. Montoya, B. Kardasz, E. Girt, Y. Y. Song, Y. Sun, and M. Wu, Spin Pumping at the Magnetic Insulator (YIG)/Normal Metal (Au) Interfaces, Phys. Rev. Lett. **107**, 066604 (2011).

[19] K. Uchida, J. Xiao, H. Adachi, J. Ohe, S. Takahashi, J. Ieda, T. Ota, Y. Kajiwara, H. Umezawa, H. Kawai, G. E. Bauer, S. Maekawa, and E. Saitoh, Spin Seebeck insulator, Nat. Mater. **9**, 894 (2010).

[20] G. E. Bauer, E. Saitoh, and B. J. Van Wees, Spin caloritronics, Nat. Mater. **11**, 391 (2012).

[21] B. L. Chittari, Y. Park, D. Lee, M. Han, A. H. MacDonald, E. Hwang, and J. Jung, Electronic and magnetic properties of single-layer M PX3 metal phosphorous trichalcogenides, Phys. Rev. B **94**, 184428 (2016).

[22] A. R. Wildes, V. Simonet, E. Ressouche, G. J. McIntyre, M. Avdeev, E. Suard, S. A. J. Kimber, D. Lançon, G. Pepe, B. Moubaraki, and T. J. Hicks, Magnetic structure of the quasi-two-dimensional antiferromagnet NiPS3, Phys. Rev. B **92**, 224408 (2015).

[23] P. Foot, J. Suradi, and P. Lee, Optical and electronic properties of the layered semiconductors $NiPS_3$ and $FePS_3$, Mater. Res. Bull. **15**, 189 (1980).

[24] J. Chu, F. Wang, L. Yin, L. Lei, C. Yan, F. Wang, Y. Wen, Z. Wang, C. Jiang, L. Feng, J. Xiong, Y. Li, and J. He, High-performance ultraviolet photodetector based on a few-layered 2D NiPS3 nanosheet, Adv. Funct. Mater. **27**, 1701342 (2017).

[25] C. C. Mayorga-Martinez, Z. Sofer, D. Sedmidubský, Š. Huber, A. Y. S. Eng, and M. Pumera, Layered metal thiophosphite materials: magnetic, electrochemical, and electronic properties, ACS Appl. Mater. Interfaces **9**, 12563 (2017).

[26] W. Zhang, J. Sklenar, B. Hsu, W. Jiang, M. B. Jungfleisch, J. Xiao, F. Y. Fradin, Y. Liu, J. E. Pearson, J. B. Ketterson, Z. Yang, and A. Hoffmann, Research Update: Spin transfer torques in permalloy on monolayer MoS_2, APL Mater. **4**, 032302 (2016).

[27] Q. Shao, G. Yu, Y.-W. Lan, Y. Shi, M.-Y. Li, C. Zheng, X. Zhu, L.-J. Li, P. K. Amiri, and K. L. Wang, Strong rashba-edelstein effect-induced spin–orbit torques in monolayer transition metal dichalcogenide/ferromagnet bilayers, Nano Lett. **16**, 7514 (2016).

[28] D. MacNeill, G. M. Stiehl, M. H. D. Guimarães, R. A. Buhrman, J. Park, and D. C. Ralph, Control of spin-orbit torques through crystal symmetry in WTe2/ferromagnet bilayers, Nat. Phys. **13**, 300 (2017).

[29] D. MacNeill, G. M. Stiehl, M. H. D. Guimarães, N. D. Reynolds, R. A. Buhrman, and D. C. Ralph, Thickness dependence of spin-orbit torques generated by WTe_2, Phys. Rev. B **96**, 054450 (2017).

[30] M. H. D. Guimarães, G. M. Stiehl, D. MacNeill, N. D. Reynolds, and D. C. Ralph, Spin–Orbit torques in $NbSe_2$/permalloy bilayers, Nano Lett. **18**, 1311 (2018).

[31] G. M. Stiehl, D. MacNeill, N. Sivadas, I. El Baggari, M. H. D. Guimarães, N. D. Reynolds, L. F. Kourkoutis, C. J. Fennie, R. A. Buhrman, and D. C. Ralph, Current-induced torques with dresselhaus symmetry due to resistance anisotropy in 2D materials, ACS Nano **13**, 2599 (2019).

[32] A. R. Mellnik, J. S. Lee, A. Richardella, J. L. Grab, P. J. Mintun, M. H. Fischer, A. Vaezi, A. Manchon, E. A. Kim, N. Samarth, and D. C. Ralph, Spin-transfer torque generated by a topological insulator, Nature (London) **511**, 449 (2014).

[33] Y. Zhang, J. Železný, Y. Sun, J. Van Den Brink, and B. Yan, Spin Hall effect emerging from a noncollinear magnetic lattice without spin-orbit coupling, New J. Phys. **20**, 073028 (2018).

[34] C.-T. Kuo, M. Neumann, K. Balamurugan, H. J. Park, S. Kang, H. W. Shiu, J. H. Kang, B. H. Hong, M. Han, T. W. Noh, and J.-G. Park, Exfoliation and raman spectroscopic fingerprint of few-layer NiPS3 van der waals crystals, Sci. Rep. **6**, 20904 (2016).

[35] See Supplemental Material at http://link.aps.org/supplemental/10.1103/PhysRevMaterials.4.084007 for the determination of the anomalous Hall resistance, additional experiments exploring the effect of the current direction on the spin-orbit torques, measurements of additional devices, temperature dependence of the anomalous Hall and planar Hall resistances, measurements of the anisotropy and exchange bias in our devices, a discussion of a possible out-of-plane dampinglike torque, and magnetometry measurements of full-sheet permalloy samples.

[36] M. Bernasconi, G. L. Marra, G. Benedek, L. Miglio, M. Jouanne, C. Julien, M. Scagliotti, and M. Balkanski, Lattice dynamics of layered MPX3 (M=Mn,Fe,Ni,Zn; X=S,Se) compounds, Phys. Rev. B **38**, 12089 (1988).

[37] K. Kim, S. Y. Lim, J.-U. Lee, S. Lee, T. Y. Kim, K. Park, G. S. Jeon, C.-H. Park, J.-G. Park, and H. Cheong, Suppression of magnetic ordering in XXZ-type antiferromagnetic monolayer NiPS3, Nat. Commun. **10**, 345 (2019).

[38] H. Matsuyama, C. Haginoya, and K. Koike, Microscopic Imaging of Fe Magnetic Domains Exchange Coupled with Those in a NiO(001) Surface, Phys. Rev. Lett. **85**, 646 (2000).

[39] U. H. Pi, K. W. Kim, J. Y. Bae, S. C. Lee, Y. J. Cho, K. S. Kim, and S. Seo, Tilting of the spin orientation induced by Rashba effect in ferromagnetic metal layer, Appl. Phys. Lett. **97**, 162507 (2010).

[40] M. Hayashi, J. Kim, M. Yamanouchi, and H. Ohno, Quantitative characterization of the spin-orbit torque using harmonic Hall voltage measurements, Phys. Rev. B **89**, 144425 (2014).

[41] A. Manchon, J. Železný, I. M. Miron, T. Jungwirth, J. Sinova, A. Thiaville, K. Garello, and P. Gambardella, Current-induced spin-orbit torques in ferromagnetic and antiferromagnetic systems, Rev. Mod. Phys. **91**, 035004 (2019).

[42] C. O. Avci, Current-induced effects in ferromagnetic heterostructures due to spin-orbit coupling, Ph.D. thesis, ETH Zurich, 2004.

[43] L. Neumann and M. Meinert, Influence of the Hall-bar geometry on harmonic Hall voltage measurements of spin-orbit torques, AIP Adv. **8**, 095320 (2018).

[44] The SOT values for D1 were corrected by dividing the obtained values by a factor of 0.67 (for $W_2/W_1 = 0.83$) and for D2 by a factor of 0.72 (for $W_2/W_1 = 0.67$) [43].

[45] G. M. Stiehl, R. Li, V. Gupta, I. E. Baggari, S. Jiang, H. Xie, L. F. Kourkoutis, K. F. Mak, J. Shan, R. A. Buhrman, and D. C. Ralph, Layer-dependent spin-orbit torques generated by the centrosymmetric transition metal dichalcogenide β-MoTe2, Phys. Rev. B **100**, 184402 (2019).

[46] M. H. Nguyen, D. C. Ralph, and R. A. Buhrman, Spin Torque Study of the Spin Hall Conductivity and Spin Diffusion Length in Platinum Thin Films with Varying Resistivity, Phys. Rev. Lett. **116**, 126601 (2016).

[47] W. Wang, T. Wang, V. P. Amin, Y. Wang, A. Radhakrishnan, A. Davidson, S. R. Allen, T. J. Silva, H. Ohldag, D. Balzar, B. L. Zink, P. M. Haney, J. Q. Xiao, D. G. Cahill, V. O. Lorenz, and X. Fan, Anomalous spin–orbit torques in magnetic single-layer films, Nat. Nanotechnol. **14**, 819 (2019).